

SPECTRAL ANALYSIS OF AN ULTRALUMINOUS X-RAY SOURCE
SWIFT J0243.6+6124

A THESIS SUBMITTED TO
THE GRADUATE SCHOOL OF NATURAL AND APPLIED SCIENCES
OF
MIDDLE EAST TECHNICAL UNIVERSITY

BY

GUBAD ISLAMOV

IN PARTIAL FULFILLMENT OF THE REQUIREMENTS
FOR
THE DEGREE OF MASTER OF SCIENCE
IN
PHYSICS

SEPTEMBER 2021

Approval of the thesis:

**SPECTRAL ANALYSIS OF AN ULTRALUMINOUS X-RAY SOURCE
SWIFT J0243.6+6124**

submitted by **GUBAD ISLAMOVI** in partial fulfillment of the requirements for the degree of **Master of Science in Physics, Middle East Technical University** by,

Prof. Dr. Halil Kalıpçılar
Dean, Graduate School of **Natural and Applied Sciences**

Prof. Dr. Seçkin Kürkcüoğlu
Head of the Department, **Physics**

Prof. Dr. Altan Baykal
Supervisor, **Physics, METU**

Examining Committee Members:

Prof. Dr. Sıtkı Çağdaş İnam
Electrical and Electronics Engineering, Başkent University

Prof. Dr. Altan Baykal
Physics, METU

Assoc. Prof. Dr. Sinan Kaan Yerli
Physics, METU

Date:

I hereby declare that all information in this document has been obtained and presented in accordance with academic rules and ethical conduct. I also declare that, as required by these rules and conduct, I have fully cited and referenced all material and results that are not original to this work.

Name Last name: Gubad Islamov

Signature:

ABSTRACT

SPECTRAL ANALYSIS OF AN ULTRALUMINOUS X-RAY SOURCE SWIFT J0243.6+6124

Islamov, Gubad
Master of Science, Physics
Supervisor: Prof. Dr. Altan Baykal

September 2021, 39 pages

In this thesis, the spectral analysis on the first galactic ultraluminous X-ray pulsar Swift J0243.6+6124 has been carried out. This peculiar object has been firstly observed by *Swift* observatory during its outburst in the late 2017 – early 2018 and it is a part of a Be/X-ray binary system. Observations obtained from NuSTAR observatory have been utilized in this study.

The analysis showed that the source underwent drastic changes from the beginning of its outburst stage, during the peak of the outburst and after the outburst. The pulse-phase-resolved spectroscopy revealed that the source was accreting in two different regimes within the span of five observations – sub-critical and super-critical ones. The phase-dependent profiles of blackbody temperature and its normalization suggest that the source has a hot spot of a certain size which indicates the existence of a sub-critical accretion in pre- and post-outburst observations. It is also shown that the object also accretes in a clumpy way during the super-critical regime. The results of the analysis are consistent with the established theory and other publications, more clarity on the accretion details of the source during its outburst stage has been achieved as a result of this thesis study.

Keywords: neutron stars, accretion regimes, pulse-phase-resolved
spectroscopy, Swift J0243.6+6124

ÖZ

AŞIRI PARLAK X-IŞINI KAYNAĞI SWIFT J0243.6+6124'ÜN TAYFSAL ANALİZİ

Islamov, Gubad
Yüksek Lisans, Fizik
Tez Yöneticisi: Prof. Dr. Altan Baykal

Eylül 2021, 39 sayfa

Bu tezde galaksimizdeki ilk aşırı parlak X-ışını atarcası Swift J0243.6+6124'ün tayfsal analizleri yapılmıştır. Bir Be/X-ışını çiftinin bir parçası olan bu tuhaf nesne, ilk defa *Swift* gözlemevi tarafından 2017 sonu – 2018 başındaki parlaması sırasında gözlemlenmiştir. Bu çalışmada ise kaynağın NuSTAR gözlemeviden alınan gözlemleri kullanılmıştır.

Yapılan analizler, kaynağın parlama başlangıcı, parlamanın tepe noktası ve parlama sonrası olmak üzere farklı evrelerde büyük değişiklikler geçirdiğini göstermiştir. Çeşitli yörünge evrelerinde yapılan tayf ölçümleri, kullanılan beş gözlemin süresi boyunca kaynağın kritik altı ve kritik üstü olmak üzere iki farklı düzende madde aktarımı yaptığını ortaya çıkarmıştır. Kara cisim sıcaklığının ve ısıl-salın normalizasyonlarının faza bağlı profilleri, kaynağın parlama öncesi ve sonrasındaki gözlemlerde kritik altı madde aktarımının varlığını gösteren belirli bir boyutta bir sıcak noktası olduğunu ortaya koymuştur. Ayrıca, kritik üstü düzende kaynağın topaklı bir şekilde madde aktarımı yaptığı gösterilmiştir. Analiz sonuçları halihazırda teori ve yayınlarla uyumlu olup, bu tez çalışmasının sonucunda kaynağın

parlama evresi esnasındaki madde aktarımı daha ayrıntılı olarak açıklığa kavuşturulmuştur.

Anahtar Kelimeler: nötron yıldızları, madde aktarım düzenleri, faz çözümlü spektroskopi, Swift J0243.6+6124

To my friends and family

ACKNOWLEDGMENTS

I would like to express my sincere gratitude to my supervisor Prof. Dr. Altan Baykal for his immense amount of support, patience and guidance. His insightful comments and feedback always motivated me to work harder and push over my limits. I would like to also thank Prof. Dr. Sıtkı Çağdaş İnam for his invaluable comments and advice during the progress of my thesis.

My research would have impossible without the aid of Dr. Muhammed Miraç Serim and all the help he provided with countless problems I have encountered. I would like to also thank my colleague Çağatay Kerem Dönmez for his help during the latest stages of my thesis progress, without that the whole process would have been much harder.

I am truly thankful to my dearest close friends and their encouragement and belief in me. Thank you for being a part of my life; I cannot imagine how unbearable it would have been without you. I would to like express my deepest gratitude to Iskender Askerov, Raheem Hashmani and Brunilda Mucogllava – our friendship is strong and firm no matter how large the distance is between us.

Most importantly, I could not have made it without my family. They always supported me in all possible ways, throughout all the years, always motivating me to move forward and never give up. I cannot express just how grateful I am to them.

TABLE OF CONTENTS

ABSTRACT.....	v
ÖZ.....	vii
ACKNOWLEDGMENTS	x
TABLE OF CONTENTS.....	xi
LIST OF TABLES	xii
LIST OF FIGURES	xiii
1 INTRODUCTION	1
1.1 Ultraluminous X-ray Sources	3
1.2 Accretion Theory	5
1.3 NuSTAR Satellite	10
2 DATA ANALYSIS.....	15
2.1 General Information about Swift J0243.6+6124	15
2.2 Data Reduction.....	16
2.3 Determination of The Pulse Period.....	18
2.4 Pulse-Phase-Averaged Spectroscopy	22
2.5 Pulse-Phased-Resolved Spectroscopy.....	25
3 DISCUSSION & CONCLUSION	31
REFERENCES	33
A. Epoch Folding Procedure.....	39

LIST OF TABLES

TABLES

Table 2.1: The coordinates and orbital parameters of the Swift J0243.6+6124 source.	16
Table 2.2: Journal of NuSTAR observations of Swift J0243.6+6124 with their respective ObsIDs, dates, exposures and count rates (from a FPMA detector), taken from Tao et al., 2019 [1]. Obs-1, Obs-2, Obs-3, Obs-4 and Obs-5 notation is introduced instead of ObsIDs in this thesis for simplicity purposes.	17
Table 2.3: The information about the spin periods of the source for the corresponding dates of NuSTAR observations taken from the Fermi database.....	19
Table 2.4: Spectral parameters that were obtained as a result of fitting the data from 5 NuSTAR observations. The radius of the region emitting blackbody R_{km} was calculated by considering that the distance to the source is 6.8 kpc [36, 37].....	23

LIST OF FIGURES

FIGURES

Figure 1.1: A diagram of a pulsar for which magnetic and rotation axis are misaligned (© Swinburne University of Technology, Centre of Astrophysics and Supercomputing (www.astronomy.swin.edu.au)).	2
Figure 1.2: The diagram of the disk accretion onto a neutron star [2].	7
Figure 1.3: The illustration of how the infalling matter accretes onto the surface of the neutron star [3].	7
Figure 1.4: The geometry of the infalling matter onto the surface of the neutron star for the cases of the “fan beam” and “pencil beam” [4].	8
Figure 1.5: A basic depiction of the accretion onto the neutron star [27].	9
Figure 1.6: The geometry of the accretion process for the super-critical case [5]. The blackbody radiation from the envelope most likely originates from the photons that were originally emitted from the neutron star and afterwards were scattered inside the cavity of the envelope before leaving it. The temperature of such blackbody radiation is on the order of 1 keV [6].	10
Figure 1.7: The image of a NuSTAR satellite and its basic structure (© 2018 NASA (www.heasarc.gsfc.nasa.gov)).	11
Figure 1.8: Comparison of the effective areas of NuSTAR and other missions [7]. As we can see from the graph, NuSTAR covers both soft and hard parts of the X-ray spectrum.	11
Figure 1.9: A 2×2 array of detectors, while each of those arrays has 32×32 pixels with a sub-millimeter size [7].	12
Figure 2.1: Lightcurves of Swift J0243.6+6124, NuSTAR observations are marked by vertical lines, taken from Tao et al., 2019 [1]. The top part of the figure corresponds to the lightcurve observed with a Swift BAT telescope; the bottom part corresponds to the one observed with Insight-HXMT telescope [1].	17

Figure 2.2: The periodograms of the source obtained from the *efsearch* task for five NuSTAR observations. The number in the brackets of the best estimated period corresponds to the 1σ error range.20

Figure 2.3: The plot of spin frequencies of the source (blue dots) obtained from the Fermi database versus time (in MJD). Red dots represent the frequencies obtained from the *efsearch* task for corresponding NuSTAR observations (from left to right): Obs-1, Obs-2, Obs-3, Obs-4, Obs-5.21

Figure 2.4: The pulse-phase-averaged energy spectra of the Obs-1, Obs-2, Obs-3, Obs-4 and Obs-5 in the 3-79 keV range. Data from both FPMA (black colored) and FPMB (red colored) detectors was used during the fitting process.....24

Figure 2.5: Unabsorbed, blackbody, power-law flux and spectral parameters (blackbody temperature, cut-off energy, photon index, radius of the region emitting blackbody and reduced χ^2 of the fit) plotted against the pulse phase for the 3-79 keV energy range. The flux values were measured in the units of 10^{-9} erg/s/cm². This figure is for Obs-1.26

CHAPTER 1

INTRODUCTION

Neutron stars are dense and compact objects that are formed when a massive star exhausts its own fuel and collapses. Main sequence stars are powered by the fusion that is happening inside their cores by burning up hydrogen. Stars that are not particularly massive can be powered by this process for billions of years and eventually arrive at the creation of white dwarfs by the end of their lifetime. Massive stars live for much shorter periods of time since they burn their fuel much faster. Within their internal structures much more massive elements are produced, up until iron. Eventually the star undergoes a supernova explosion and after that, the remaining compact object can be either a neutron star or a black hole. If the mass of the progenitor star is approximately in the range from 8 to $25 M_{\odot}$, it will likely produce a neutron star at the end; the cores of more massive stars collapse into black holes. Typically, the masses of neutron stars are roughly located in the range between $1 - 2 M_{\odot}$ and they have a radius of approximately 10 km [8]. Generally, the mass of a usual neutron star is approximated to $1.4 M_{\odot}$.

Neutron stars are often observed near the centers of supernova remnants and they emit electromagnetic radiation in radio, optical, X-ray and gamma ray bands. They can also be observed as pulsars which are rapidly spinning neutron stars with strong magnetic fields. X-ray pulsars can be detected in binary systems where a neutron star is accreting material from a companion star and emit radiation [9]. Accreting material is directed by the field lines toward the magnetic poles, as the material loses gravitational energy electromagnetic radiation is produced along the magnetic poles. Generally, scientists assume that accretion-powered pulsars have magnetic fields of dipolar form and their strength is $\sim 10^{12} - 10^{13}$ G [10]. The whole range of possible

values for magnetic field strengths is larger, starting from $\sim 10^8$ G for millisecond pulsars up to $> 10^{15}$ G for magnetars [11].

Pulsars were firstly observed in 1967 by Bell and Hewish [12], when Jocelyn Bell, a graduate student at that time, noticed periodic radio pulsations from a strange source. At the time, there was an uncertainty in the nature of the source as scientists were not sure about it. However, Gold argued that the source should be a rotating neutron star with a strong magnetic field [13]. He predicted that the rotational period of these objects should be increasing as the rotational energy was lost as the radiation which was later confirmed as scientists discovered this property in the period of the Crab pulsar [8]. After the discovery by Bell and Hewish [12], many other objects with similar properties were observed and they were called “pulsars”. A very common scenario for a pulsar is when the rotation axis and the magnetic axis are misaligned; the light beam from the magnetic poles is rotating together with the neutron star. If this beam of light sweeps Earth during the rotation period, astronomers can detect a pulse that give the rotational period [9]. A common diagram for pulsars is presented in Figure 1.1:

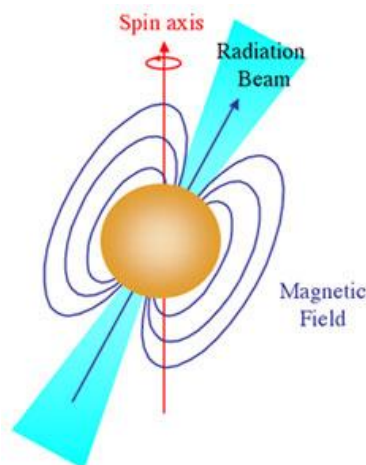


Figure 1.1: A diagram of a pulsar for which magnetic and rotation axis are misaligned (© Swinburne University of Technology, Centre of Astrophysics and Supercomputing (www.astronomy.swin.edu.au)).

1.1 Ultraluminous X-ray Sources

Ultraluminous X-ray sources (or, shortly, ULXs) appear to be extremely bright objects assuming that the emission is isotropic and they are mostly found in other external galaxies. Most of the ULXs are considered to be X-ray binary systems where the accretion process onto a compact object takes place and their luminosities are at the same level or even higher than the Eddington luminosity of stellar black holes [14]. One of the important aspects of such sources is the nature of the objects in those binary systems – the compact object itself and the companion star. Together with the orbital geometry, they are all related to the observed X-ray, radio and other types of the electromagnetic radiation as well as the physics behind the accretion rate in those systems [14].

First ULXs were observed with the launch of the first X-ray imaging telescope - Einstein observatory (HEAO-2) in 1978 [15]. This observatory was able to set a difference between active galactic nuclei and ULXs due to its specifications [16]. The first cases of ULXs were reported in 1981 in which a source with a high luminosity was observed in M33 galaxy with a luminosity of roughly 10^{39} erg s^{-1} [17]. Later, other X-ray sources with a similar level of luminosity were found in other nearby galaxies, like M31 and Maffei 1 [18]. Typically, a certain luminosity threshold is defined for an object to be classified as an ULX, in most cases it is 1×10^{39} erg s^{-1} which is a very convenient definition [14]. If the source has a luminosity above 1×10^{41} erg s^{-1} [19], it is defined as a “hyperluminous X-ray source”, a term which was first used in Matsumoto et al., (2004) [20]. Such a source could potentially be an intermediate mass black hole [14].

The list of the most famous ULXs is provided below:

- **M82 X-1:** An ultraluminous X-ray source considered to be an intermediate-mass black hole which is located in M82 galaxy. It is known for its high

luminosity levels which can reach even 10^{41} erg s⁻¹. The mass of the supposed black hole is considered to be in the interval of 300 – 800 solar masses [21].

- **M82 X-2:** An ultraluminous X-ray pulsar (or, shortly, ULP) also located in M82 galaxy with luminosity levels of $10^{38} - 10^{40}$ erg s⁻¹ that shows a variation on a period of roughly 60 days [21]. The spin period of the source is roughly 1.4 seconds [22].
- **Holmberg II X-1:** An ultraluminous X-ray source located in a dwarf galaxy of an irregular shape. It is assumed that this source is an intermediate-mass black hole with a maximum mass estimate of approximately 1000 solar masses [23].
- **M101 X-1:** An ultraluminous X-ray source located in the M101 galaxy. This source is considered to be a black hole with a large radius of emission during its high luminosity phases of 10^{39} erg s⁻¹. High luminosity phases are separated by long and low luminosity phases of roughly 10^{37} erg s⁻¹ [24].

When it comes to ultraluminous X-ray pulsars, there is a clear evidence for super-Eddington accretion to be taking place as their measured peak luminosities exceed Eddington limit several times [14]. In general Eddington limit is defined as the luminosity for a spherical object of mass M at which the gravitational attraction of this object is balanced by the outward force of the radiation. It can be calculated as:

$$L_{edd} = \frac{4\pi GcMm_p}{\sigma_T} \quad (1.1)$$

where G is the gravitational constant, c is the speed of light, m_p is the mass of a proton, σ_T is the Thomson scattering cross-section [25] and it is measured in the units of erg s⁻¹. For instance, a pulsar NGC 5907 ULX exceeds this limit by roughly 500 times [16]. A necessary requirement for super-Eddington accretion to take place is

the fact that there must be a high enough mass transfer rate onto a compact object [14]:

$$\dot{m} = \frac{L_{bol}}{\eta c^2} \quad (1.2)$$

where \dot{m} is the mass transfer rate, L_{bol} is the bolometric luminosity and η is the radiative efficiency of the accretion process which is usually taken usually as 0.1 for the conversion of mass to radiation with little outflow process [14]. In that case, the mass transfer rate that is necessary for reaching the bolometric luminosity of approximately 10^{39} erg s⁻¹, is roughly $1.8 \times 10^{-7} M_{\odot} \text{ yr}^{-1}$. On the other hand, taking the expression for the Eddington luminosity of the compact object as [14]:

$$L_{edd} \simeq 1.3 \times 10^{38} M_{co} \text{ erg s}^{-1} \quad (1.3)$$

where M_{co} is the mass of the compact object in terms of the solar masses; the transfer rate of the mass \dot{m} that is necessary to reach the Eddington limit itself is $2.3 \times 10^{-8} M_{co} M_{\odot} \text{ yr}^{-1}$ [14]. One possible mechanism by which the mass transfer rate may reach high enough values in order to surpass the Eddington limit is when the companion star of the compact object starts to expand and fills the Roche lobe in high mass X-ray binaries [26]. For both black holes and neutron stars, the mass transfer rates can be high enough to exceed the Eddington limit by multiple times [14].

1.2 Accretion Theory

The development of a physical model which would explain the super-Eddington accretion process onto a neutron star can be pretty complex. It is considered that the magnetic field strength of a neutron star must play a crucial role in it. At the Alfvén radius r_A of the neutron star, the magnetic pressure of a neutron star is balanced by the so-called *ram* pressure, which is defined as the pressure that the infalling matter

exerts upon the magnetic field. The Alfvén radius r_A can be calculated in the following way:

$$r_A \simeq 2.6 \times 10^8 \times \mu_{30}^{\frac{4}{7}} \left(\frac{M}{M_\odot} \right)^{\frac{1}{7}} L_{37}^{-\frac{2}{7}} R_6^{-\frac{2}{7}} \text{ cm} \quad (1.4)$$

where μ_{30} is the magnetic moment which is measured in the units of 10^{30} G cm^3 , L_{37} is the luminosity of the accretion process measured in the units of $10^{37} \text{ erg s}^{-1}$, R_6 is the radius of the source measured in the units of 10^6 cm and M is its mass [27].

Matter can accrete onto the surface of the compact object as it starts following the magnetic field lines at about the Alfvén radius and it accretes directly onto the magnetic poles. The representation of this process is illustrated on Figure 1.2. On that schematic diagram, for radii smaller than the inner disc radius the matter will follow magnetic field lines and abandon the disk, a process that starts at the boundary layer with the width of $r_0 - r_A$. In the transition zone, the matter moves across the residual field of the source and it produces screening currents that screen the magnetic field to a radius r_s , which is much larger than the Alfvén radius of the neutron star. For radii larger than r_s , the flow of the matter is not disturbed by the magnetic field.

For strong magnetic fields, the matter accretes onto the surface via accretion column or accretion funnel. Due to this geometry, the Eddington limit can be exceeded since the radiation can escape at the sides of the funnel [14]. If the magnetic field is particularly strong in the vicinity of the funnel, such field may prevent the motion that is perpendicular to the field lines of the magnetic field of the electrons in the accretion flow, the cross-section will be reduced such that it is lower than the Thomson value for the photons that are polarized perpendicularly to the magnetic field. This may be another way to overcome the Eddington limit [14].

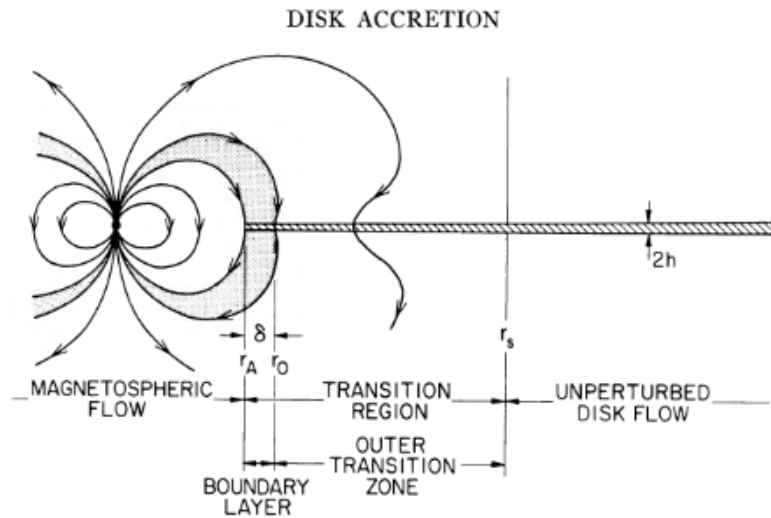


Figure 1.2: The diagram of the disk accretion onto a neutron star [2].

Figure 1.3 depicts how the radiation escapes from the funnel and tends to move sideways from the base of the funnel. However, since the infalling material accretes onto the neutron at a very high speed, the escaped radiation can also move downwards and reflect from the surface and then move in the upward direction; such process would result in a radiative cone [3].

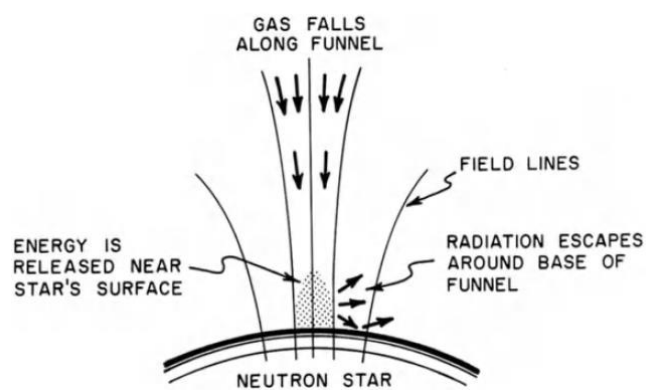


Figure 1.3: The illustration of how the infalling matter accretes onto the surface of the neutron star [3].

Depending on how much material is accreting onto the neutron star, there are two expected geometries of the resulting electromagnetic radiation. If the amount of material that is falling onto the star is low, the infalling matter will heat the surface of the neutron star and the surface will emit X-rays with a blackbody spectrum; the direction of this radiation will be antiparallel to the direction of the infalling matter, such geometry is the so-called “pencil beam”. On the other hand, if the amount of infalling material onto the neutron star is high, a shock-front will prevent the “pencil beam” type of radiation so that the only way for the radiation to escape will be via the sides of the column. Such geometry is the so-called “fan beam” structure [28]. Both of these geometries are illustrated in the Figure 1.4:

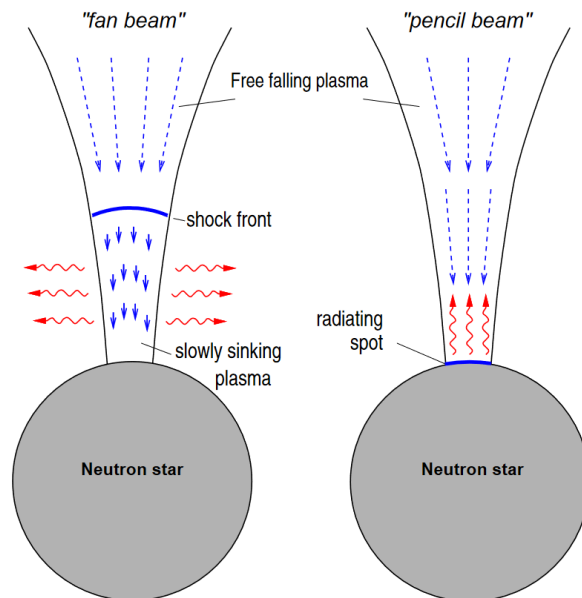


Figure 1.4: The geometry of the infalling matter onto the surface of the neutron star for the cases of the “fan beam” and “pencil beam” [4].

In the case of sub-critical (sub-Eddington) accretion regime, the matter will accrete onto the neutron stars via the magnetic lines and form “hot spots” on the magnetic poles. The areas of these hot spots are on the order of 1 km^2 , as it can be inferred from Figure 1.5:

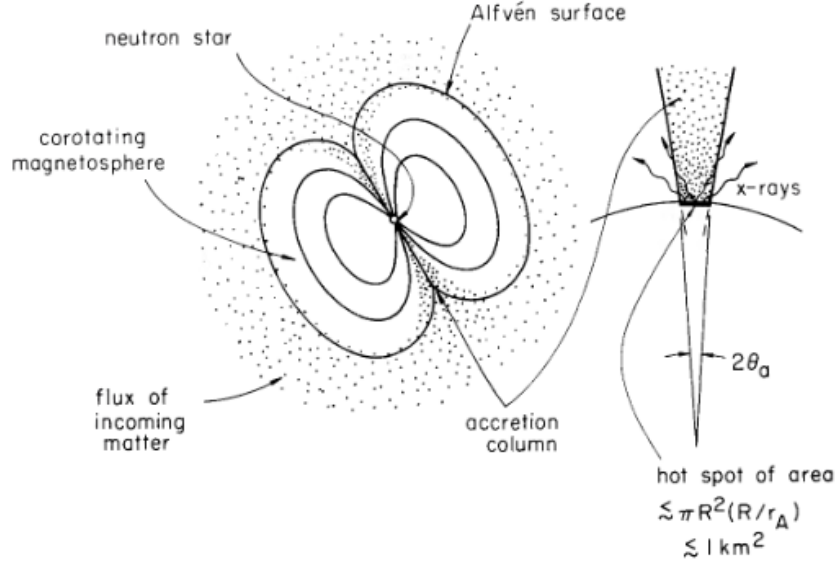


Figure 1.5: A basic depiction of the accretion onto the neutron star [27].

Super-critical (super-Eddington) accretion regime typically occurs when the accretion rate is high and the luminosity of the accretion corresponds to:

$$L \geq 3.4 \times 10^{38} m^{\frac{6}{11}} B_{12}^{\frac{6}{11}} \Lambda^{\frac{21}{22}} \text{ erg s}^{-1} \quad (1.5)$$

where Λ is a constant which depends on the geometry of the accretion and it is typically taken as 0.5, B_{12} is the strength of the surface magnetic field measured in units of 10^{12} G, $m = \frac{M}{M_{\odot}}$ is the mass of the neutron star measured in the units of solar masses [6]. When such luminosities are achieved, the accretion disk becomes geometrically thick [6]. In this case, the neutron star becomes surrounded by an optically thick envelope, as illustrated in Figure 1.6:

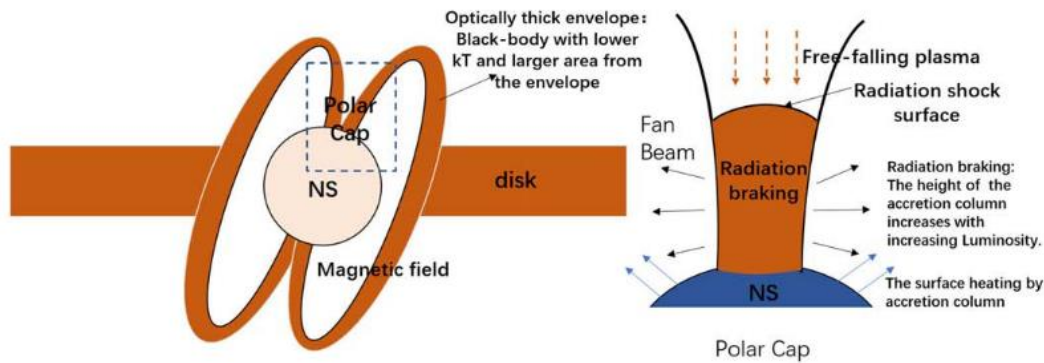


Figure 1.6: The geometry of the accretion process for the super-critical case [5]. The blackbody radiation from the envelope most likely originates from the photons that were originally emitted from the neutron star and afterwards were scattered inside the cavity of the envelope before leaving it. The temperature of such blackbody radiation is on the order of 1 keV [6].

1.3 NuSTAR Satellite

The Nuclear Spectroscopic Telescope Array (NuSTAR) is a satellite astronomy mission specifically designed to cover harder energies of X-ray spectrum and it was launched in June, 2012 onto a low-Earth orbit with an operating lifetime of roughly 10 years [7]. It was the first telescope array that was designed by the use of solid-state detectors that allowed observations at energies higher than 10 keV. NuSTAR, for the time of its launch, allowed scientists to probe energies up to 79 keV, its whole operating energy range is 3-79 keV. One of the primary objectives of the NuSTAR mission include the investigation of active galactic nuclei as well as studying the population of X-ray sources in the Milky Way and the investigation of the emissions from supernova remnants [7]. The image of the satellite and its basic structure is shown on Figure 1.7; Figure 1.8 shows the effective collecting area of NuSTAR and its comparison with other missions:

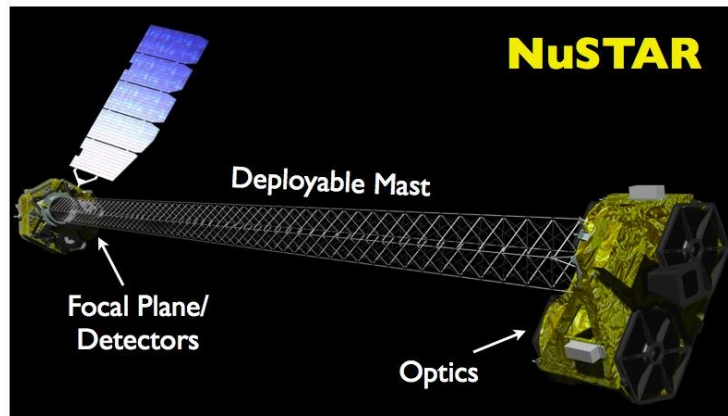


Figure 1.7: The image of a NuSTAR satellite and its basic structure (© 2018 NASA (www.heasarc.gsfc.nasa.gov)).

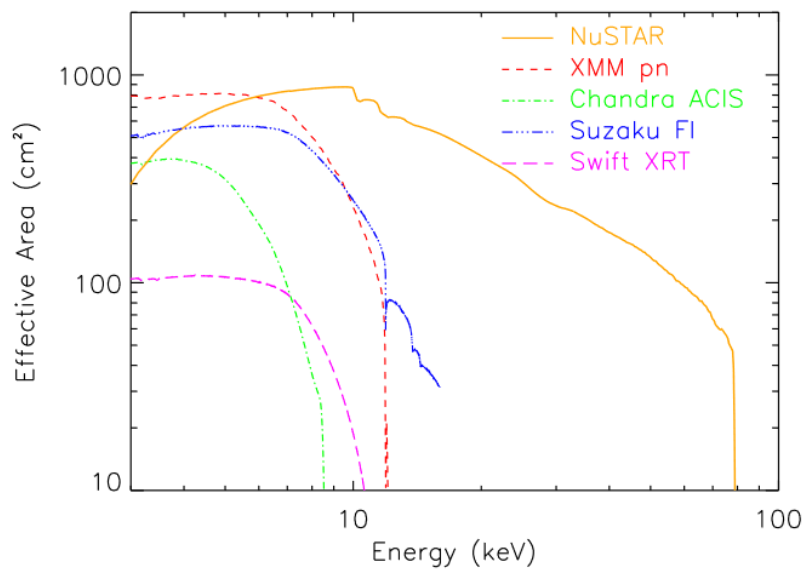


Figure 1.8: Comparison of the effective areas of NuSTAR and other missions [7]. As we can see from the graph, NuSTAR covers both soft and hard parts of the X-ray spectrum.

X-ray optics of NuSTAR is comprised of 133 grazing incidence shells; the optics is coated with specific multilayer structures that increase the graze for a significant reflectance for energies above 15 keV. As a result, the field of view and the collecting

area is increased. 89 inner shells are coated with Pt/C multilayers that reflect at energies below 78.4 keV, other 44 outer shells are coated with W/Si multilayers that reflect at energies below 69.5 keV [7]. Photons of those energies are reflected on CdZnTe detectors which are placed at two focal plane modules, FPMA and FPMB. The field of view is $12'$ which is achieved by a 2×2 array of detectors, while each of those arrays has 32×32 pixels; an image of this array of detectors is shown on Figure 1.9. The time of the events that is registered by these detectors has an accuracy of $2 \mu\text{s}$ relative to an on-board clock. The mast of the satellite separates the detectors and the X-ray optics by roughly 10 m that is the focal length separation. It is made out of specific material that has low thermal expansion coefficient but the mast is still subject to slight disturbances due to extreme thermal conditions on the orbit. These disturbances cause a slight motion of the optical axis and the X-ray focal point on the focal plane; this slight motion is on the orders of a few millimeters per orbit [7].

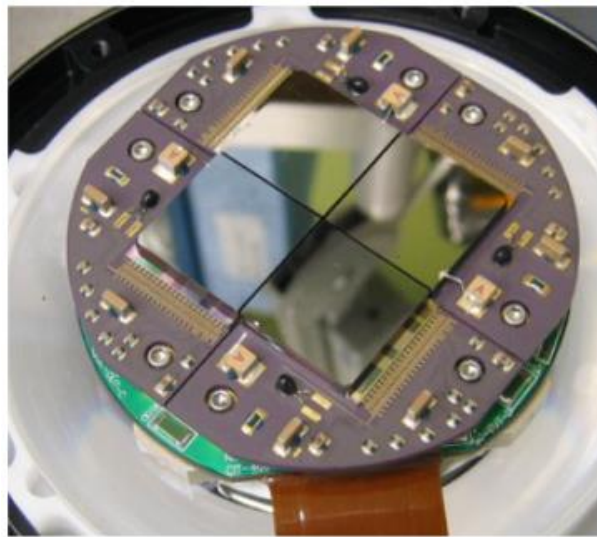


Figure 1.9: A 2×2 array of detectors, while each of those arrays has 32×32 pixels with a sub-millimeter size [7].

For the data analysis of NuSTAR observations a NuSTAR Data Analysis Software (NuSTARDAS) software has been designed which is fully compatible with the

HEASoft software. The software carries out specific tasks for the calibration of the data, data screening and the extraction of products such as energy spectra, lightcurves, RMF and ARF files [7].

CHAPTER 2

DATA ANALYSIS

2.1 General Information about Swift J0243.6+6124

Swift J0243.6+6124 is an ultraluminous X-ray pulsar and it is the first one of its type that was detected in our galaxy [29]. This source was discovered by the *Swift* observatory during its outburst in 2017-2018 [30]. At first, it was considered to be a gamma ray burst [31]. However, as more observations of this source were made, ≈ 9.8 s pulsations were detected from it [30, 32], which established it as a pulsating neutron star [33]. This object is showing a spin-up for luminosities higher than 10^{39} erg s^{-1} [34]. The whole system is also identified to be a Be/X-ray binary system due to the detection of hydrogen and helium lines on the optical spectrum of the companion [35]. The distance to this source which was measured by *Gaia* is roughly 6.8 kpc [36, 37]. The magnetic field was not calculated precisely so far since no cyclotron features were detected by NuSTAR and Insight-HXMT observations of this source [37]. By analyzing luminosity levels of the source, scientists estimate that the magnetic field strength of Swift J0243.6+6124 should be on the order of $10^{12} - 10^{13}$ G [37, 38]. The spectrum of the source has been analyzed for this source in various literature. Jaisawal et al., 2017 performed phase-averaged and phase-resolved analysis of one of the NuSTAR observations [39]; Jaisawal et al., 2019 analyzed the combined spectra of the source from NICER and NuSTAR satellites [29]. Tao et al., 2019 analyzed five NuSTAR observations of the source and made a spectral fit of the data with different blackbody models in order to explain the physical processes happening in the vicinity of the source [1]. The key parameters of the

source are shown below in Table 2.1; the values of these parameters were reported in the Fermi database (www.gammaray.nsstc.nasa.gov):

Table 2.1: The coordinates and orbital parameters of the Swift J0243.6+6124 source.

Parameter	Value
Right Ascension	40.9180°
Declination	61.4341°
Orbital Period	27.7 days
Period Derivative	0.00E+00 days/day
$T_{\pi/2}$	2458116.097 (JED)
$a_x \sin(i)$	115.531 light-s
Long. of periastron	-74.05°
Eccentricity	0.1029

2.2 Data Reduction

In this work five NuSTAR observations during the outburst of the source in the late 2017 – early 2018 were analyzed. The IDs of these observations, their dates, exposures and count rates are shown in the Table 2.2. These observations are also shown as vertical gray lines in the Figure 2.1, which illustrates the light-curves of the source obtained from the *Swift* and Insight-HXMT observatories.

Table 2.2: Journal of NuSTAR observations of Swift J0243.6+6124 with their respective ObsIDs, dates, exposures and count rates (from a FPMA detector), taken from Tao et al., 2019 [1]. Obs-1, Obs-2, Obs-3, Obs-4 and Obs-5 notation is introduced instead of ObsIDs in this thesis for simplicity purposes.

ObsID	Obs.	Date	Date (in MJD)	Exposure (s)	Count Rate (counts/s)
90302319002	Obs-1	Oct 5 2017	58031	14277	122.78 ± 0.09
90302319004	Obs-2	Oct 31 2017	58057	1293	2700.3 ± 1.5
90302319006	Obs-3	Nov 10 2017	58067	676	4001 ± 2
90302319008	Obs-4	Dec 6 2017	58093	4589	959.5 ± 0.5
90401308002	Obs-5	Mar 10 2018	58187	27816	16.88 ± 0.03

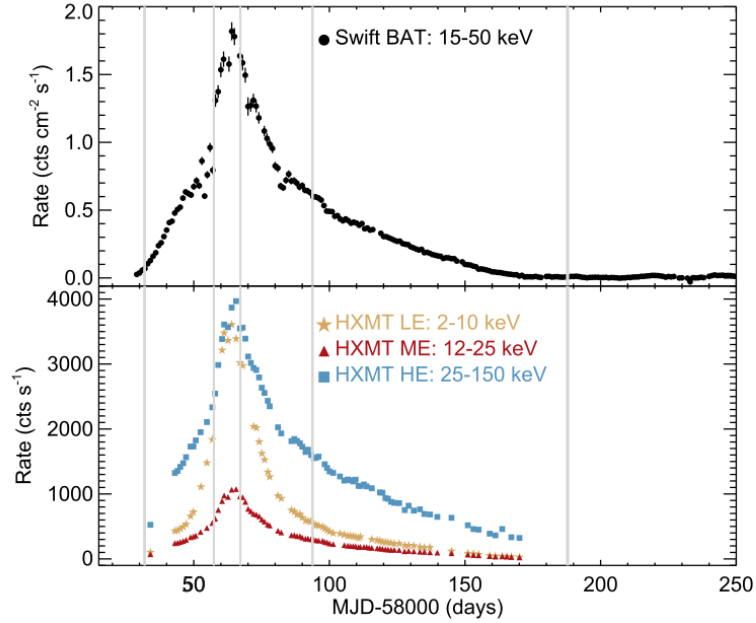


Figure 2.1: Lightcurves of Swift J0243.6+6124, NuSTAR observations are marked by vertical lines, taken from Tao et al., 2019 [1]. The top part of the figure corresponds to the lightcurve observed with a Swift BAT telescope; the bottom part corresponds to the one observed with Insight-HXMT telescope [1].

The analysis of these observations was carried out by using NuSTARDAS v2.0.0 software which is implemented in the HEASoft v6.28 with the CALDB version of 20201217. Cleaned event files were generated by using the task *nupipeline* version 0.4.8. However, a necessary command has to be added in the *nupipeline* task (except the last NuSTAR observation, Obs-5) during the generation of the cleaned event files in order to keep the source events which could have been omitted due to the high count rate ($> 100 \text{ counts s}^{-1}$) [40]. Following the analysis method of Tao et al., 2019 [1], the source events were by setting a circular region of the $180''$ radius. The background was also estimated from a region where the source was absent of the same radius.

2.3 Determination of The Pulse Period

Precise spin periods had to be considered in this thesis study in order to perform pulse-phase-resolved spectroscopy for five different NuSTAR observations due to the fact that spin period is changing over the time span of the outburst. For this purpose, the data from the Fermi database (www.gammaray.nsstc.nasa.gov), containing the information about the evolution of the spin frequency of the source with respect to time (which was recorded in MJD) was analyzed and the necessary spin frequencies for five NuSTAR observations were considered. The information about the dates of the observations and the corresponding spin periods of Swift J0243.6+6124 are given in Table 2.3. The errors were calculated by considering the frequency errors taken from the Fermi database and by utilizing the following formula:

$$\frac{\Delta P}{P} = \frac{\Delta f}{f} \quad (5.1)$$

where f , Δf and P are the frequencies, errors in frequencies and periods respectively.

Table 2.3: The information about the spin periods of the source for the corresponding dates of NuSTAR observations taken from the Fermi database.

Observation	The date of the observation (MJD)	Spin period (s)
Obs-1	58031	9.853959(8)
Obs-2	58057	9.8428323(1)
Obs-3	58067	9.8257518(2)
Obs-4	58093	9.8038246(6)
Obs-5	58187	9.79137(2)

Barycentric and orbital corrections has been applied to the time columns in the event files of five different NuSTAR observations by using the parameters given in Table 2.1 which were obtained from the Fermi database. After the barycentric correction has been applied by utilizing the *barycorr* parameter in the *nuproducts* task, and the orbital correction has been applied by utilizing *fcalc* task, the period values have been checked by using the *efsearch* task. *Efsearch* task is a part of an epoch-folding procedure (see Appendix A).

The results of this task are the periodograms on which the possible period values are estimated by utilizing the χ^2 -statistics according to a pre-defined resolution (0.1×10^{-2} s in this study). The peak of the χ^2 distribution corresponds to the best value for the spin period of the source. The number of phase bins per period was set to be 16 for all 5 observations. The error for the estimated period was calculated by using the following formula:

$$\Delta P = \frac{P^2}{nT} \quad (5.2)$$

where P is the best estimated period value, n is the number of phase bins and T is the time span of the observation [41]. Figure 2.2 shows the periodograms obtained in this study for five NuSTAR observations:

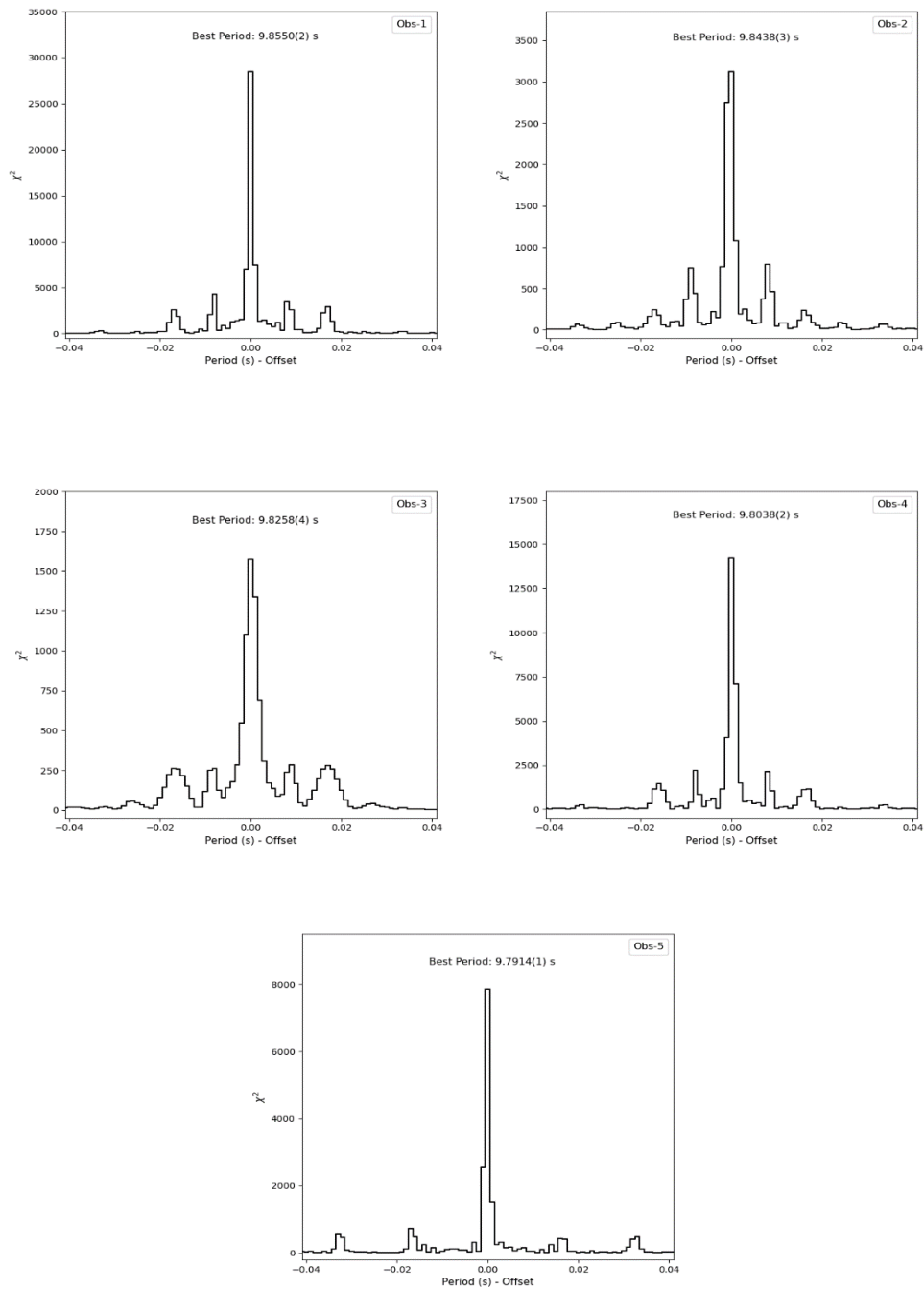


Figure 2.2: The periodograms of the source obtained from the *efsearch* task for five NuSTAR observations. The number in the brackets of the best estimated period corresponds to the 1σ error range.

We can compare the periods that were obtained by using the *efsearch* task and the periods directly obtained from Fermi database in the Figure 2.3:

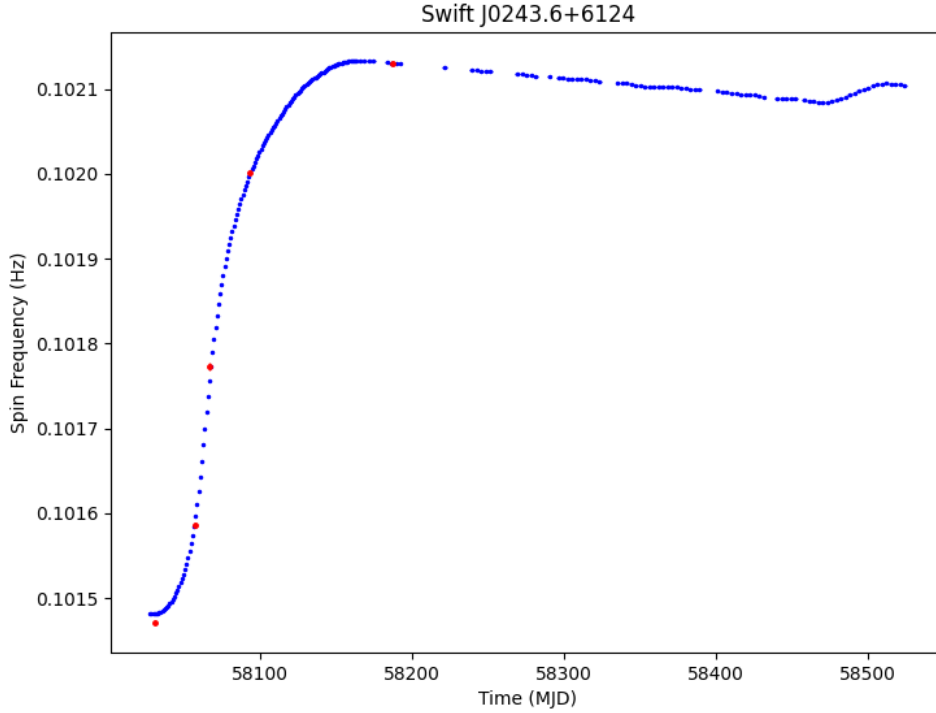


Figure 2.3: The plot of spin frequencies of the source (blue dots) obtained from the Fermi database versus time (in MJD). Red dots represent the frequencies obtained from the *efsearch* task for corresponding NuSTAR observations (from left to right): Obs-1, Obs-2, Obs-3, Obs-4, Obs-5.

As it can be seen in the Figure 2.3, in general there is a good agreement with the curve obtained from the Fermi database and the results of the *efsearch* task. The *efsearch* frequency values for Obs-3, Obs-4 and Obs-5 are consistent with the frequencies obtained from the Fermi database within 1σ error range. The *efsearch* frequency values for Obs-1 and Obs-2 are not consistent with the frequencies obtained from the Fermi database due to the fact that the latter measurements include only 1st and 2nd harmonics while measurements from *efsearch* include more harmonics. In

order to keep the analysis more precise and safer, the pulse-phase-resolved spectroscopy was performed by utilizing the frequency values that were obtained from the Fermi database.

2.4 Pulse-Phase-Averaged Spectroscopy

Source and background spectra were extracted by using *nuproducts* package and grouped with *grppha* task to have 64 counts per bin to achieve a good signal-to-noise ratio. Pulse-phase-averaged spectra in the 3-79 keV range were analyzed by using XSPEC v12.11.1 package. The data has been modeled with an absorption model *tbabs* [42], a blackbody model with a normalization that is proportional to the area of the emitting surface *bbodyrad*, a power-law exponential cut-off model *cutoffpl*, a gaussian line model *gauss* for Fe K α emission lines, and for the observations Obs-2, Obs-3 and Obs-4, an additional absorption edge model *edge* was required to fit the data for Fe K-edge at 7.1 keV. For the phase-averaged spectroscopy of the Obs-1 and Obs-5 the *tbabs*(cutoffpl+bodyrad+gauss)* model was used, while for the Obs-2, Obs-3 and Obs-4 the *tbabs*edge*(cutoffpl+bodyrad+gauss+gauss)* model was used with the addition of the *edge* model component.

During the modeling of the data, the hydrogen column density, N_H parameter, was kept frozen at the value of 7.0×10^{21} atoms/cm² for Obs-2, Obs-3 and Obs-4 which is the value of the parameter in the direction of the source [43]. The iron line energies were fixed at 6.42 and 6.67 keV as it was performed in the analysis carried out by Jaisawal et al., 2019 [29]. The radius of the region emitting blackbody R_{km} was calculated by utilizing the following expression:

$$BB \text{ normalization} = \frac{R_{km}^2}{D^2} \quad (2.1)$$

where R_{km} is the radius of the region emitting blackbody in km, *BB normalization* is the blackbody normalization and D is the distance to the source measured in the

units of 10 kpc [44]. The best-fit values of spectral parameters are shown in the Table 2.4. Alongside with this table of spectral parameters, the energy spectra of 5 NuSTAR observations are included in the Figure 2.4.

Table 2.4: Spectral parameters that were obtained as a result of fitting the data from 5 NuSTAR observations. The radius of the region emitting blackbody R_{km} was calculated by considering that the distance to the source is 6.8 kpc [36, 37].

Component	Parameter	Obs-1	Obs-2	Obs-3	Obs-4	Obs-5
<i>tbabs</i>	N_H	0.77 ± 0.15	0.7 (fixed)	0.7 (fixed)	0.7 (fixed)	$1.39^{+0.32}_{-0.31}$
<i>cutoffpl</i>	Γ	1.09 ± 0.03	$1.25^{+0.03}_{-0.04}$	$1.41^{+0.02}_{-0.03}$	0.74 ± 0.02	1.19 ± 0.05
	E_{cut} (keV)	$24.1^{+0.9}_{-0.8}$	$20.2^{+0.5}_{-0.6}$	21.3 ± 0.5	17.2 ± 0.2	$24.7^{+1.7}_{-1.5}$
	norm.	0.28 ± 0.01	$9.78^{+0.67}_{-0.72}$	$21.91^{+1.03}_{-1.09}$	1.53 ± 0.05	0.05 ± 0.01
<i>bbodyrad</i>	kT (keV)	3.05 ± 0.03	0.81 ± 0.01	$1.00^{+0.05}_{-0.04}$	0.78 ± 0.01	2.18 ± 0.05
	R_{km}	0.97 ± 0.01	$54.72^{+1.31}_{-1.30}$	$25.96^{+2.79}_{-2.83}$	$28.24^{+0.79}_{-0.81}$	0.57 ± 0.03
<i>gauss</i>	E (keV)	6.46 ± 0.04	6.42 (fixed)	6.42 (fixed)	6.42 (fixed)	6.38 ± 0.04
	σ (keV)	0.45 ± 0.07	$1.94^{+0.17}_{-0.11}$	$1.66^{+0.05}_{-0.04}$	1.72 ± 0.05	$0.20^{+0.12}_{-0.10}$
<i>gauss</i>	E (keV)		6.67 (fixed)	6.67 (fixed)	6.67 (fixed)	
	σ (keV)		$1.01^{+0.14}_{-0.15}$	$0.43^{+0.15}_{-0.09}$	$0.43^{+0.10}_{-0.06}$	
<i>edge</i>	E_{edge} (keV)		7.01 ± 0.02	$6.99^{+0.03}_{-0.04}$	$6.87^{+0.04}_{-0.06}$	
	τ		0.16 ± 0.01	0.10 ± 0.01	0.09 ± 0.01	
	$\chi^2/d.o.f.$	1.17	1.22	1.11	1.33	1.24

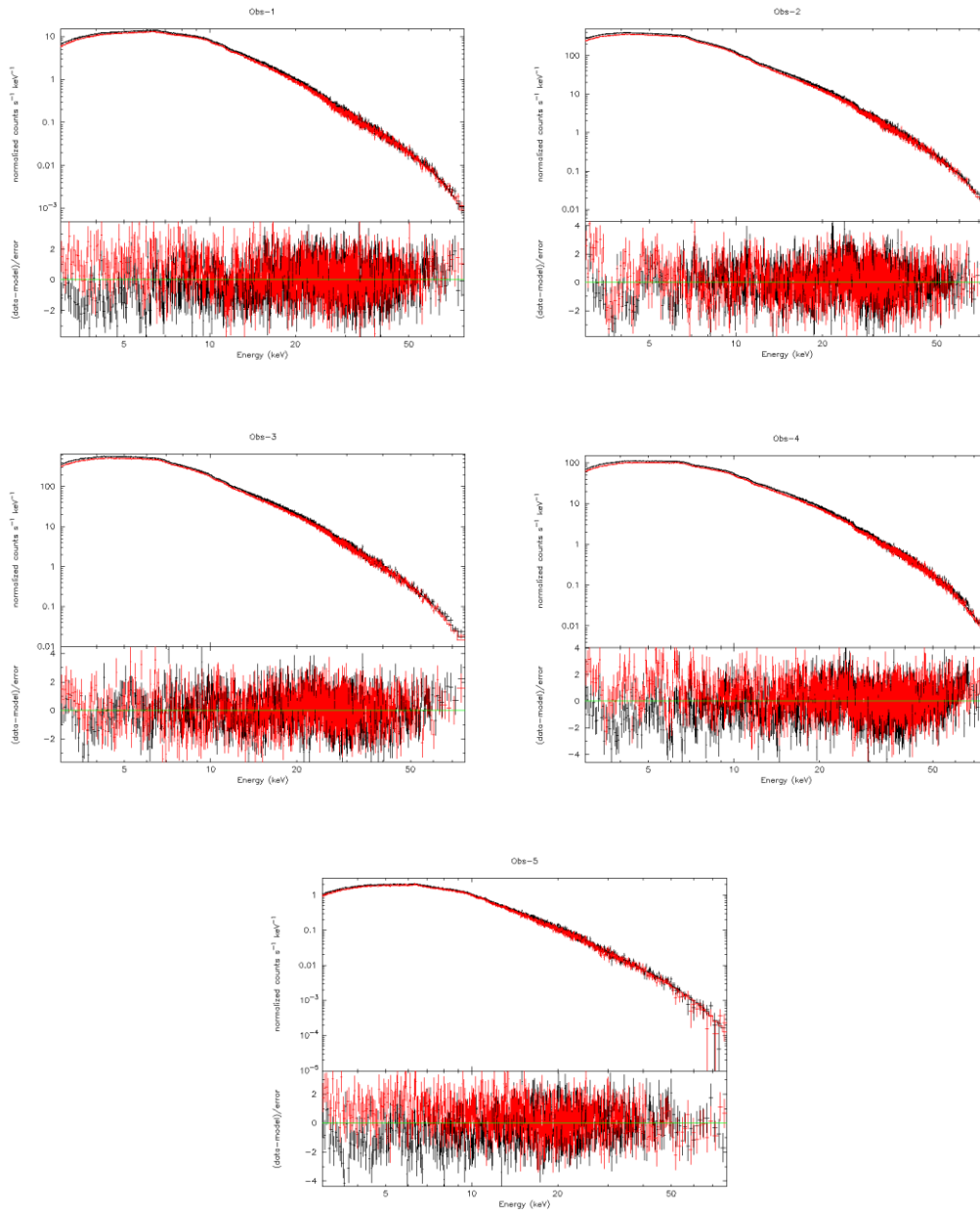


Figure 2.4: The pulse-phase-averaged energy spectra of the Obs-1, Obs-2, Obs-3, Obs-4 and Obs-5 in the 3-79 keV range. Data from both FPMA (black colored) and FPMB (red colored) detectors was used during the fitting process.

2.5 Pulse-Phased-Resolved Spectroscopy

Pulse-phase-resolved spectroscopy was performed for all NuSTAR observations in order to understand the geometry of the emission of the source. For that purpose, XSELECT v2.4k package was used to obtain phase-sliced spectra in 16 phase bins. Same effective area files and response matrices that were used for pulse-phase-averaged spectroscopy were used in this analysis. The analysis was carried over the 3-79 keV range and data from both FPMA and FPMB detectors was used for the spectroscopy. For the pulse-phase-resolved spectroscopy same models which are defined in section 3.1 were used except for Obs-2, Obs-3 and Obs-4 where only a singular *gauss* model was used for the iron emission line at 6.42 keV. The flux values were calculated by using the *cflux* model.

During the modeling of the data, the hydrogen column density, N_H parameter, was kept frozen at the value of 7.0×10^{21} atoms/cm² for all 5 observations and the iron line energy was kept frozen at a specific value for Obs-1 and Obs-5 as it is reported in Tao et al., 2019 [1]. For Obs-5, the width of the iron line energy was kept frozen as well. The values were adopted from the reported values from the Tao et al., (2019) [1]. Variation of best-fit spectral parameters over pulse phase are shown below on the Figure 2.5 (Cont'd) for each respective observation:

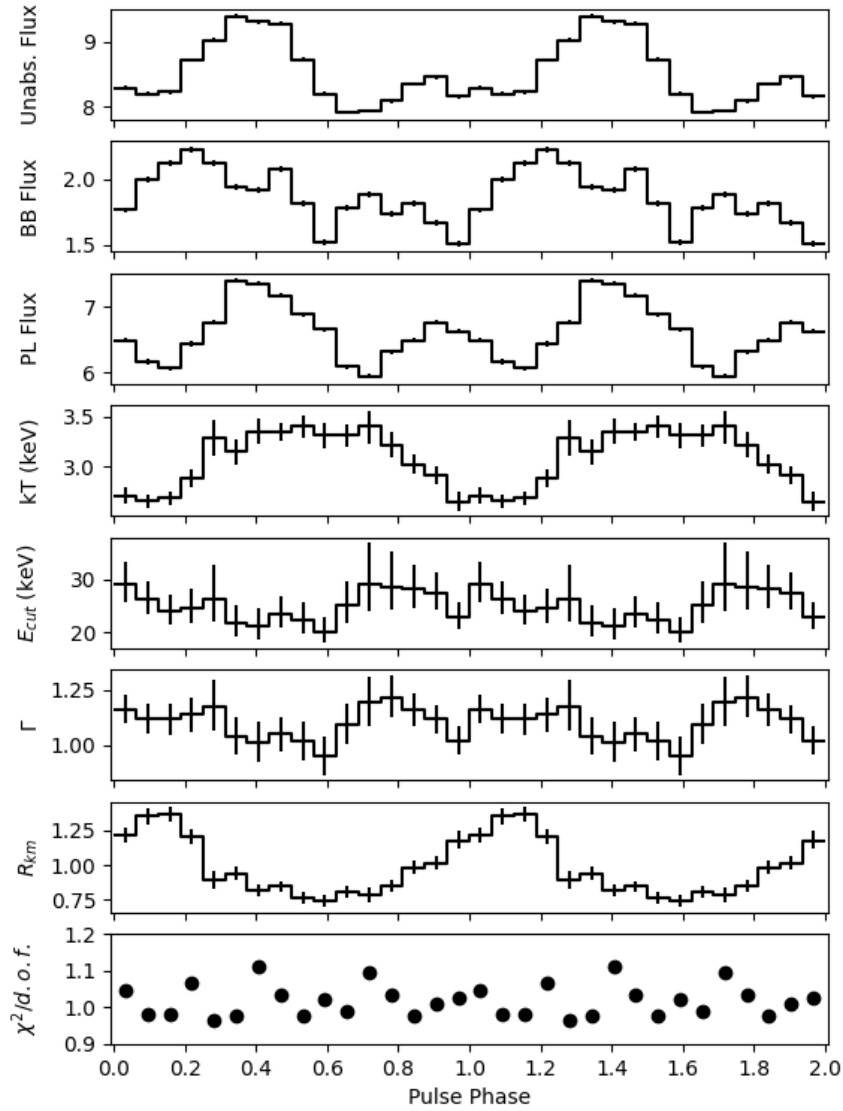


Figure 2.5: Unabsorbed, blackbody, power-law flux and spectral parameters (blackbody temperature, cut-off energy, photon index, radius of the region emitting blackbody and reduced χ^2 of the fit) plotted against the pulse phase for the 3-79 keV energy range. The flux values were measured in the units of 10^{-9} erg/s/cm². This figure is for Obs-1.

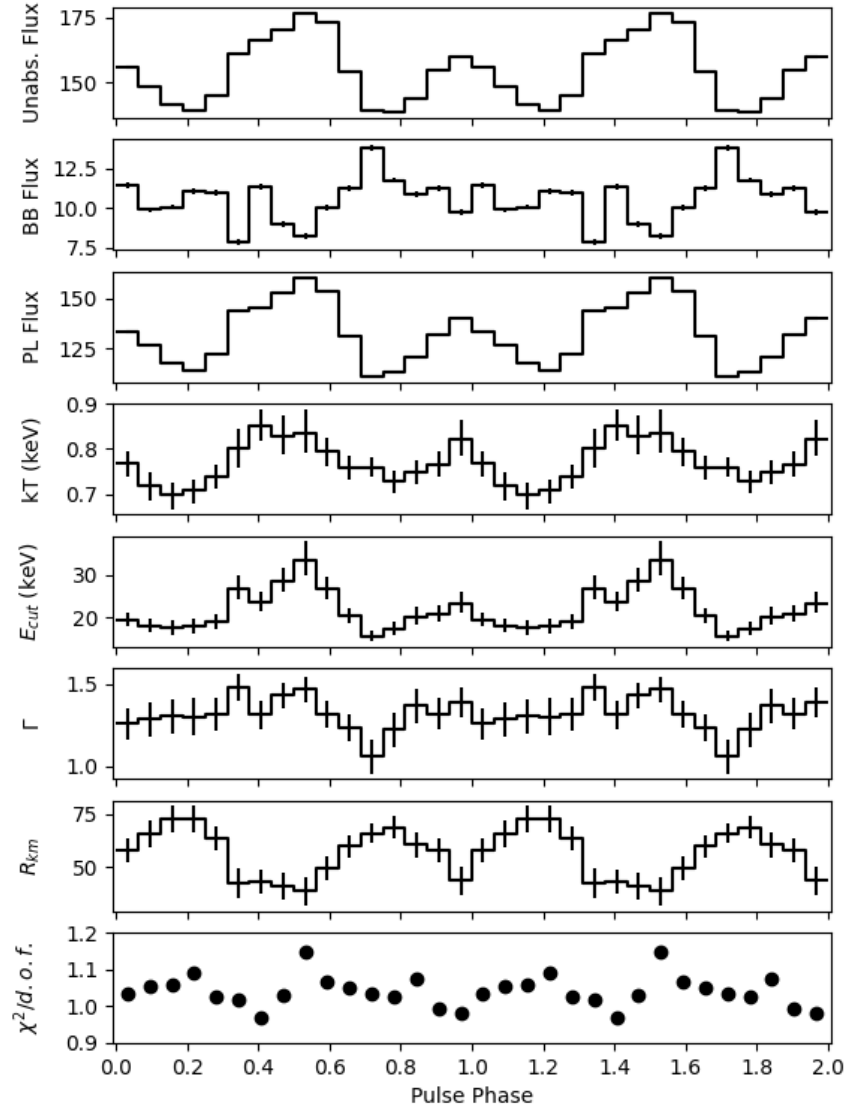


Figure 2.5 (Cont'd): This figure is for Obs-2.

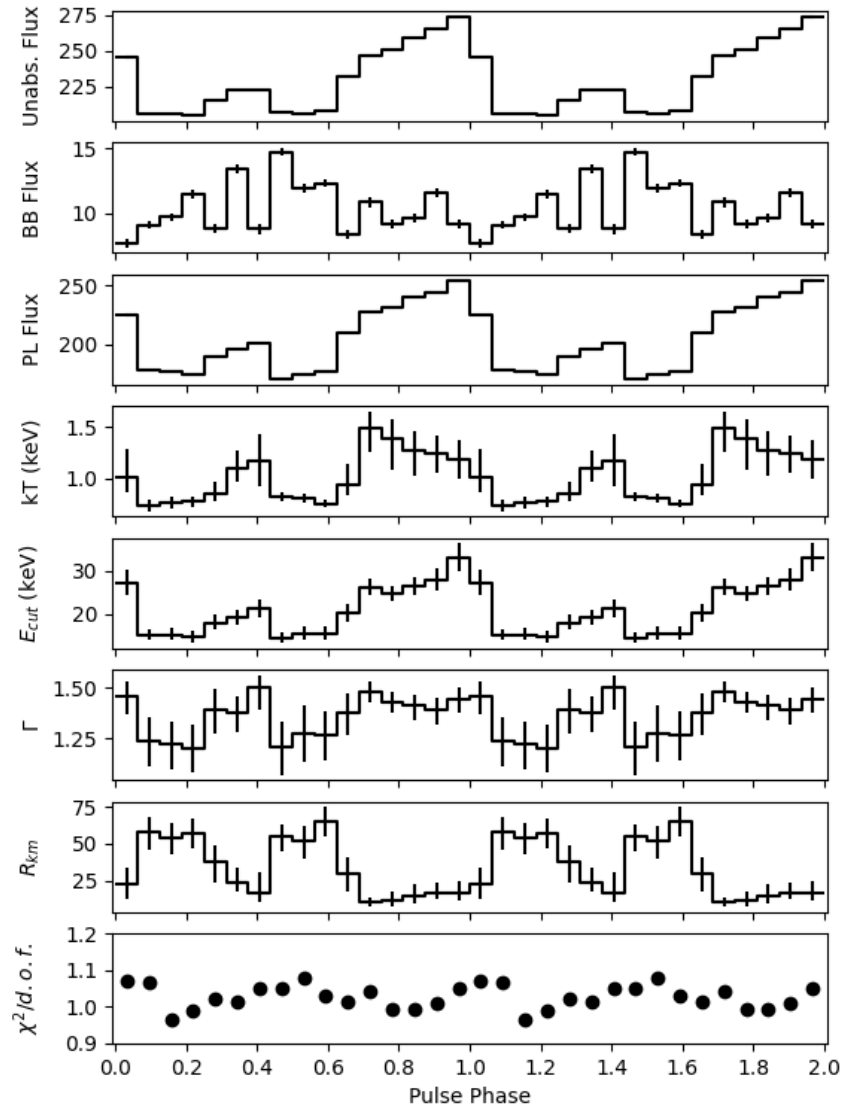


Figure 2.5 (Cont'd): This figure is for Obs-3.

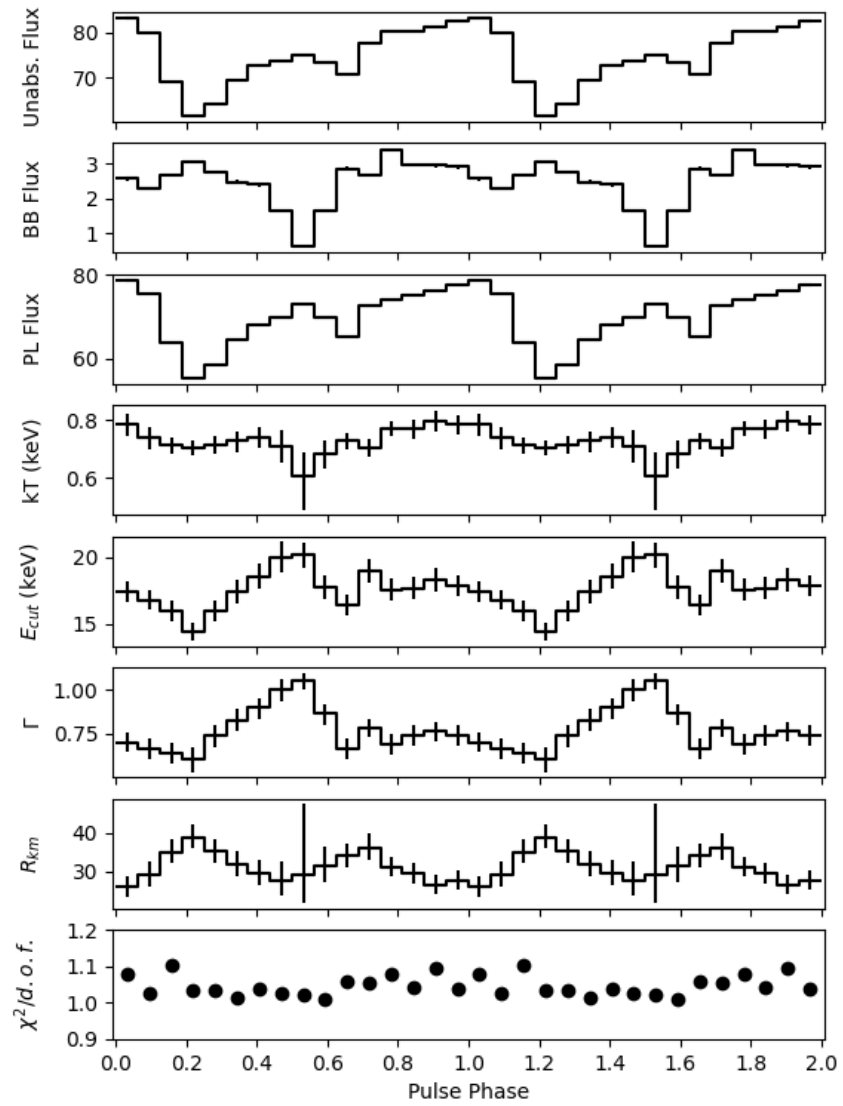


Figure 2.5 (Cont'd): This figure is for Obs-4.

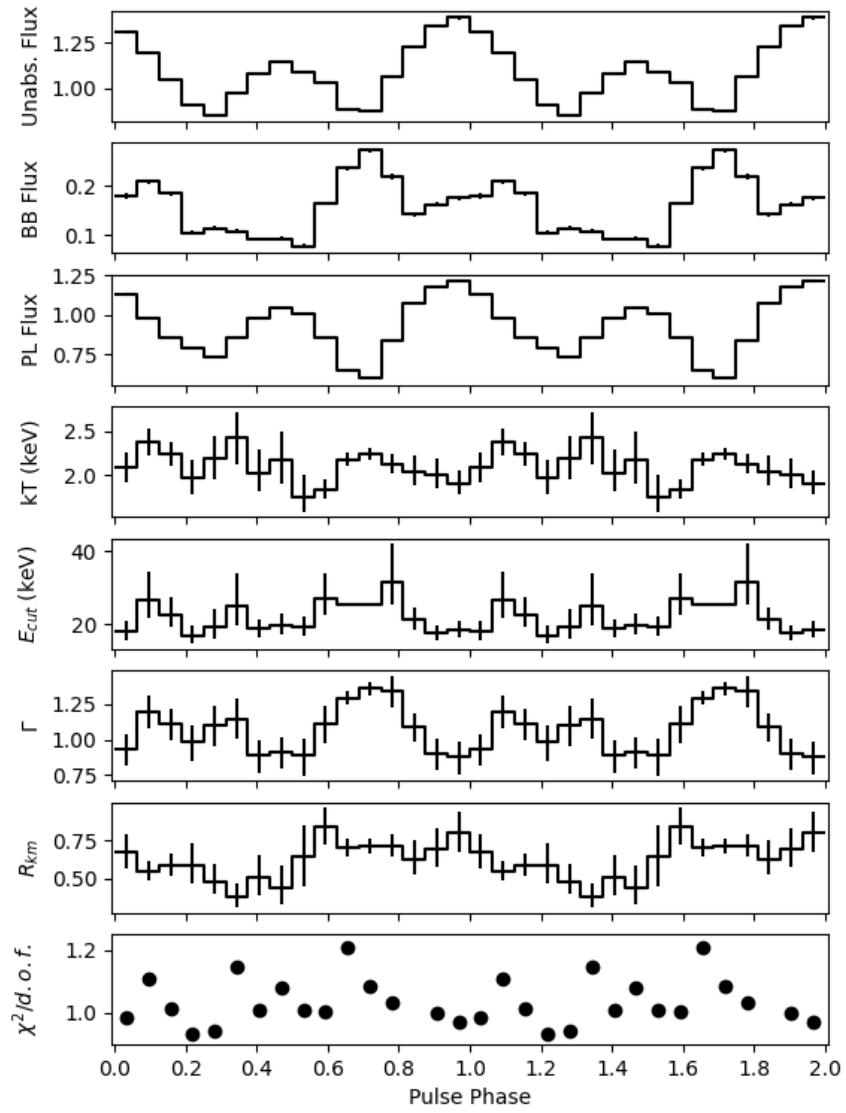


Figure 2.5 (Cont'd): This figure is for Obs-5.

CHAPTER 3

DISCUSSION & CONCLUSION

In this study, pulse-phase-averaged and pulse-phase-resolved spectroscopy analyses have been performed on five different NuSTAR observations. Spectral plots have been produced, the values of flux and parameters as well as their dependencies on pulse phase have been plotted. Although a phase-resolved analysis was done for only the 1st NuSTAR observation previously [39], all of the five observations are analysed here in order to identify spectral variations in different outburst stages (pre- and post-outburst ones).

In general, as we can see from Figure 2.5 (Obs-1), Figure 2.5 (Obs-2), Figure 2.5 (Obs-3), Figure 2.5 (Obs-4) and Figure 2.5 (Obs-5) the shapes of unabsorbed flux profiles are mostly characterized by the power-law (PL) flux which suggests that non-thermal emission is the main source of the radiation while the blackbody (BB) emission contributes very little to the unabsorbed flux.

By comparing the values of flux and parameters on Figure 2.5 (Obs-1) and Figure 2.5 (Obs-5), it can be inferred that the source is accreting in one specific regime in those epochs. Same argument can be made by comparing Figure 2.5 (Obs-2), Figure 2.5 (Obs-3) and Figure 2.5 (Obs-4). The analysis of the luminosity evolution of the spectra was studied by Kong et al., 2020 [5] with Insight-HXMT data and the finding of this thesis confirms their results.

From Figure 2.5 (Obs-1) and Figure 2.5 (Obs-5), one can conclude that the source is accreting in the sub-critical regime due to the fact that the blackbody (BB) temperature is on the order of ~ 3 keV and the values for the radii of the region emitting blackbody are pretty low. In this regime emission from the poles of the neutron star has pencil beam geometry (see Figure 1.4). As it can be seen from Figure

2.5 (Obs-1) and Figure 2.5 (Obs-5), the radius of the region emitting blackbody is on the order of 1 keV, which is a reasonable size of a hot spot for a neutron star accreting in a sub-critical regime (as it can be seen from Figure 1.5).

Another interesting outcome of the results from Figure 2.5 (Obs-1) and Figure 2.5 (Obs-5) is that while unabsorbed and power-law fluxes tend to be low at their respective phases (the dependency of these fluxes on phase is almost identical), the blackbody flux tends to be around its maxima (or close to it). This feature could be explained in the following way – while unabsorbed flux is maximum, mostly non-thermal emission is observed, however, when the unabsorbed flux is minimum, more thermal emission from the hot spot on a neutron star surface is observed.

In the case of Figure 2.5 (Obs-2), Figure 2.5 (Obs-3) and Figure 2.5 (Obs-4) – the values of the flux get significantly higher and, consequently, the radius of the region emitting blackbody gets higher while the BB temperature gets lower than they are in low flux observations (first and the last ones); these temperatures are on the order of 1 keV or less [5]. One could conclude that in this case the source is accreting in the super-critical regime. The thermal emission can no longer originate solely from the hot spot anymore, the values for the radii of the region emitting blackbody are bigger than the radius of the neutron star itself. In fact, this emission could be originating from a thick envelope that would surround the source in this regime (as it can be seen in Figure 1.6). Then, one would expect a more or less uniform BB emission that would be independent on the pulse phase. According to Figure 2.5 (Obs-2), Figure 2.5 (Obs-3) and Figure 2.5 (Obs-4), some small variations in the radius of the region emitting blackbody (or BB temperature, conversely) profiles are observed, this could be explained if we assume that the temperature distribution in the envelope material is slightly uneven due to the clumpy accretion process onto the neutron star [45].

REFERENCES

- [1] L. Tao *et al.*, “Super-Eddington Accretion onto the Galactic Ultraluminous X-Ray Pulsar Swift J0243.6+6124,” *The Astrophysical Journal*, vol. 873, no. 1, p. 19, Feb. 2019.
- [2] P. Ghosh and F. K. Lamb, “Disk accretion by magnetic neutron stars,” *The Astrophysical Journal*, vol. 223, p. L83, Jul. 1978.
- [3] K. Davidson and J. P. Ostriker, “Neutron-Star Accretion in a Stellar Wind: Model for a Pulsed X-Ray Source,” *The Astrophysical Journal*, vol. 179, p. 585, Jan. 1973.
- [4] Evolution Of X-Ray Binaries, College Park, Md (United States), 11-13 Oct 1993, Related Information: Aip Conference Proceedings, No. 308 [Apcpcs, S. S. Holt, and C. S. Day, *The evolution of x-ray binaries*. New York, Ny (United States); Aip, 1994.
- [5] L. D. Kong *et al.*, “Two Complete Spectral Transitions of Swift J0243.6+6124 Observed by Insight-HXMT,” *The Astrophysical Journal*, vol. 902, no. 1, p. 18, Oct. 2020.
- [6] A. A. Mushtukov, V. F. Suleimanov, S. S. Tsygankov, and A. Ingram, “Optically thick envelopes around ULXs powered by accreting neutron stars,” *Monthly Notices of the Royal Astronomical Society*, p. stx141, Jan. 2017.
- [7] F. A. Harrison *et al.*, “THE NUCLEAR SPECTROSCOPIC TELESCOPE ARRAY (NuSTAR) HIGH-ENERGY X-RAY MISSION,” *The Astrophysical Journal*, vol. 770, no. 2, p. 103, May 2013.
- [8] I. Vidaña, “A short walk through the physics of neutron stars,” *The European Physical Journal Plus*, vol. 133, no. 10, Oct. 2018.
- [9] NASA, “Neutron Stars, Pulsars, and Magnetars - Introduction,” *Nasa.gov*, 2017. https://imagine.gsfc.nasa.gov/science/objects/neutron_stars1.html (accessed Sep. 23, 2021).

- [10] C. Y. Cardall, M. Prakash, and J. M. Lattimer, “Effects of Strong Magnetic Fields on Neutron Star Structure,” *The Astrophysical Journal*, vol. 554, no. 1, pp. 322–339, Jun. 2001.
- [11] S. Konar, “Magnetic Fields of Neutron Stars,” *Journal of Astrophysics and Astronomy*, vol. 38, no. 3, Sep. 2017.
- [12] A. HEWISH, S. J. BELL, J. D. H. PILKINGTON, P. F. SCOTT, and R. A. COLLINS, “Observation of a Rapidly Pulsating Radio Source,” *Nature*, vol. 217, no. 5130, pp. 709–713, Feb. 1968.
- [13] T. GOLD, “Rotating Neutron Stars as the Origin of the Pulsating Radio Sources,” *Nature*, vol. 218, no. 5143, pp. 731–732, May 1968.
- [14] P. Kaaret, H. Feng, and T. P. Roberts, “Ultraluminous X-Ray Sources,” *Annual Review of Astronomy and Astrophysics*, vol. 55, no. 1, pp. 303–341, Aug. 2017.
- [15] “The High Energy Astrophysics Observatory 2 (Einstein),” [heasarc.gsfc.nasa.gov. https://heasarc.gsfc.nasa.gov/docs/einstein/heo2.html](https://heasarc.gsfc.nasa.gov/docs/einstein/heo2.html) (accessed Aug. 05, 2021).
- [16] K. Atapin, “Ultraluminous X-ray Sources,” *Proceedings of Accretion Processes in Cosmic Sources – II — PoS(APCS2018)*, Feb. 2019.
- [17] K. S. Long, S. Dodorico, P. A. Charles, and M. A. Dopita, “Observations of the X-ray sources in the nearby SC galaxy M33,” *The Astrophysical Journal*, vol. 246, p. L61, Jun. 1981.
- [18] G. Fabbiano, “X Rays From Normal Galaxies,” *Annual Review of Astronomy and Astrophysics*, vol. 27, no. 1, pp. 87–138, Sep. 1989.
- [19] Y. Gao, Q. D. Wang, P. N. Appleton, and R. A. Lucas, “Nonnuclear Hyper/Ultraluminous X-Ray Sources in the Starbursting Cartwheel Ring Galaxy,” *The Astrophysical Journal*, vol. 596, no. 2, pp. L171–L174, Sep. 2003.
- [20] H. Matsumoto, I. Tatsuya, T. G. Tsuru, S. Matsushita, K. Watarai, and S. Mineshige, “Peculiar Characteristics of the Hyper-Luminous X-Ray Source M82 X-1,” *Progress of Theoretical Physics Supplement*, vol. 155, pp. 379–380, 2004.
- [21] M. Brightman et al., “Spectral Evolution of the Ultraluminous X-Ray Sources M82 X-1 and X-2,” *The Astrophysical Journal*, vol. 889, no. 1, p. 71, Jan. 2020.

- [22] G. Collura et al., “Search for Optical Pulsation in M82 X-2,” *The Astrophysical Journal*, vol. 850, no. 1, p. 65, Nov. 2017.
- [23] D. Cseh et al., “Unveiling recurrent jets of the ULX Holmberg II X-1: evidence for a massive stellar-mass black hole.” *Monthly Notices of the Royal Astronomical Society: Letters*, vol. 439, no. 1, pp. L1–L5, Jan. 2014.
- [24] R.-F. Shen, R. Barniol Duran, E. Nakar, and T. Piran, “The nature of ULX source M101 X-1: optically thick outflow from a stellar mass black hole,” *Monthly Notices of the Royal Astronomical Society: Letters*, vol. 447, no. 1, pp. L60–L64, Dec. 2014.
- [25] J. Fukue, “Eddington limit for a gaseous stratus with finite optical depth,” *Publications of the Astronomical Society of Japan*, vol. 67, no. 3, p. 57, Jun. 2015.
- [26] A. R. King, M. B. Davies, M. J. Ward, G. Fabbiano, and M. Elvis, “Ultraluminous X-Ray Sources in External Galaxies,” *The Astrophysical Journal*, vol. 552, no. 2, pp. L109–L112, May 2001.
- [27] F. K. Lamb, C. J. Pethick, and D. Pines, “A Model for Compact X-Ray Sources: Accretion by Rotating Magnetic Stars,” *The Astrophysical Journal*, vol. 184, p. 271, Aug. 1973.
- [28] H. Klus, *How We Came to Know the Cosmos: Space & Time*, 2nd ed. The Star Garden, 2018.
- [29] G. K. Jaisawal et al., “An Evolving Broad Iron Line from the First Galactic Ultraluminous X-Ray Pulsar Swift J0243.6+6124,” *The Astrophysical Journal*, vol. 885, no. 1, p. 18, Oct. 2019.
- [30] J. A. Kennea et al., “Swift J0243.6+6124: Swift discovery of an accreting NS transient,” *The Astronomer’s Telegram*, vol. 10809, p. 1, 2017.
- [31] S. B. Cenko et al., *GRB Coordinates Network, Circular Service*, No. 21960, #1-2018, 21960, 2017.
- [32] P. Jenke and C. A. Wilson-Hodge., “Fermi GBM detects pulsations from Swift J0243.6+6124,” *The Astronomer’s Telegram*, vol. 10812, p. 1, 2017.

- [33] A. Bahramian, J. A. Kennea and A. W. Shaw, “Swift and NuSTAR observations of Swift J0243.6+6124,” *The Astronomer’s Telegram*, vol. 10866, p. 1, 2017.
- [34] V. Doroshenko, S. Tsygankov, and A. Santangelo, “Orbit and intrinsic spin-up of the newly discovered transient X-ray pulsar Swift J0243.6+6124,” *Astronomy & Astrophysics*, vol. 613, p. A19, May 2018.
- [35] K. Kouroubatzakis, P. Reig, J. Andrews and A. Zezas, “The optical counterpart to the new accreting pulsar Swift J0243.6+6124 is a Be star”, *The Astronomer’s Telegram*, vol. 10822, p. 1, 2017.
- [36] C. A. Wilson-Hodge et al., “NICER and Fermi GBM Observations of the First Galactic Ultraluminous X-Ray Pulsar Swift J0243.6+6124,” *The Astrophysical Journal*, vol. 863, no. 1, p. 9, Aug. 2018.
- [37] V. Doroshenko et al., “Hot disk of the Swift J0243.6+6124 revealed by Insight-HXMT,” *Monthly Notices of the Royal Astronomical Society*, Oct. 2019.
- [38] S. S. Tsygankov, V. Doroshenko, A. A. Mushtukov, A. A. Lutovinov, and J. Poutanen, “On the magnetic field of the first Galactic ultraluminous X-ray pulsar Swift J0243.6+6124,” *Monthly Notices of the Royal Astronomical Society: Letters*, vol. 479, no. 1, pp. L134–L138, Jun. 2018.
- [39] G. K. Jaisawal, S. Naik, and J. Chenevez, “Understanding the spectral and timing behaviour of a newly discovered transient X-ray pulsar Swift J0243.6+6124,” *Monthly Notices of the Royal Astronomical Society*, vol. 474, no. 4, pp. 4432–4437, Dec. 2017.
- [40] “NuSTAR Frequently Asked Questions,” *heasarc.gsfc.nasa.gov*. https://heasarc.gsfc.nasa.gov/docs/nustar/nustar_faq.html (accessed Sep. 22, 2021).
- [41] M. M. Serim, “Pulse timing studies of X-ray binaries: GX1+4, SWIFT J0513.4-6547, X Persei and SXP 1062,” Ph.D. Thesis, Middle East Technical University, 2019.
- [42] J. Wilms, A. Allen, and R. McCray, “On the Absorption of X-Rays in the Interstellar Medium,” *The Astrophysical Journal*, vol. 542, no. 2, pp. 914–924, Oct. 2000.

- [43] “HEASARC: X-Ray Background Tool v3.0: Calculate Average X-Ray Background Count Rates from RASS Maps,” *heasarc.gsfc.nasa.gov*. <https://heasarc.gsfc.nasa.gov/cgi-bin/Tools/xraybg/xraybg.pl> (accessed Sep. 22, 2021).
- [44] “bbodyrad: blackbody spectrum, area normalized,” *heasarc.gsfc.nasa.gov*. <https://heasarc.gsfc.nasa.gov/xanadu/xspec/manual/node137.html> (accessed Aug. 05, 2021).
- [45] D. R. Pasham and T. E. Strohmayer, “EVIDENCE FOR QUASI-PERIODIC X-RAY DIPS FROM AN ULTRALUMINOUS X-RAY SOURCE: IMPLICATIONS FOR THE BINARY MOTION,” *The Astrophysical Journal*, vol. 764, no. 1, p. 93, Jan. 2013.
- [46] D. A. Leahy *et al.*, “On searches for pulsed emission with application to four globular cluster X-ray sources - NGC 1851, 6441, 6624, and 6712,” *The Astrophysical Journal*, vol. 266, p. 160, Mar. 1983.

APPENDIX

A. Epoch Folding Procedure

Epoch folding (or e-folding, shortly) procedure is a part of a timing analysis of the astronomical data in which a light curve of the data with an observational time span T is “folded” and summed over an initially guessed value of periodicity P [46]. This periodicity is split into n number of phase bins and the light curve is split into segments of equal time durations $\Delta t_i = P/n$; subscript i stands for the index introduced for each phase bin (it starts with 1 and goes up to n). Normalized count rates S_i can be obtained by summing over the count rates in the “modulus” segments [41]:

$$S_i = \frac{1}{M} \sum_{j=0}^{M-1} S_{\Delta t_{i+jn}} \quad (\text{A.1})$$

where M is the maximum number of cycles for a data of the specific length.

The profile of S_i vs i is called a pulse profile. Depending on how well the initial guess for periodicity P was given, the shape of the pulse profile may be different. The χ^2 -statistics is used in this case to determine the best periodicity:

$$\chi^2 = \sum_{i=1}^n \frac{(S_i - \bar{S})^2}{\sigma_i^2} \quad (\text{A.2})$$

where σ_i is the uncertainty of a particular count rate in a bin and \bar{S} is the average count rate. The best periodicity will yield the highest values of χ^2 , other periodicities will have a lower value.